

Extensions and Applications of Holographic Particle Characterization

by

Mark D. Hannel

A dissertation submitted in partial fulfillment

of the requirements for the degree of

Doctor of Philosophy

Department of Physics

New York University

September, 2018

David G. Grier

© Mark D. Hannel

All Rights Reserved, 2018

Dedication

To anyone weary soul who comes across this.

Acknowledgments

The Ph.D. has been pleasure and a pain. Thanks to the people who never let me quit despite my desperate pleas!

Abstract

Contents

Dedication	iv
Acknowledgments	v
Abstract	vi
List of Figures	ix
List of Tables	xiii
1 Introduction	1
2 Holographic characterization of imperfect colloidal spheres	2
2.1 Introduction	2
2.2 Holographic particle characterization	2
3 Machine-learning approach to holographic particle characteriza-	
tion	14
3.1 Introduction	14
3.2 Fast Holographic Characterization with Machine Learning	15
3.3 Characterization of Colloidal Mixtures	20

3.4	Tracking and Assessment of Precision	22
3.5	Conclusions	25
4	Machine-learning techniques for fast and accurate feature localization in holographic images	27
4.1	Introduction: Holographic Particle Characterization	27
4.2	Detecting and Localizing Holographic Features	29
4.3	Holographic Image Formation	33
4.4	Applying Machine Learning to Holographic Particle Localization . .	36
4.5	Discussion	46
5	Optimizing the synthesis of monodisperse colloidal spheres	48
5.1	Experimental Section	49
5.2	Results and discussion	52
5.3	Conclusion	52
6	Conclusions	55
	Bibliography	56

List of Figures

2.3 Holographic characterization of dimpled TPM spheres with radius $a_p = 0.5 \mu\text{m}$ as a function of dimple radius a_d and center-to-center distance, d . (a) Relative error in holographically estimated radius. (b) Relative error in refractive index. Plot symbols indicate shape of dimpled spheres.	11
3.1 Colloidal characterization by holographic microscopy and machine learning. Colloidal spheres flowing down a microfluidic sample scatter light from a collimated laser beam to form an in-line hologram. Features in the beam are identified, and their radial profiles presented to support vector machines (SVMs) that compare them with a library of training data to estimate each spheres' radius a_p and refractive index n_p . The scatter plot shows results for 2,500 spheres drawn at random from a mixture of four different types of spheres. Each point is colored by the local density of data points, $\rho(a_p, n_p)$. . .	16
3.2 Tracking and characterizing a single colloidal sphere. (a) The estimated axial position $z_p(t)$ relative to the focal plane of the microscope of a single polystyrene sphere sedimenting through water as it diffuses. The line is a least-squares fit. Insets show the sphere's hologram at the beginning and end of the trajectory. (b) The radius a_p and refractive index n_p estimated from each hologram in the same sequence, colored by time. Each dot corresponds to values obtained from a single hologram. (c) The mean-squared displacement, $\Delta z_p^2(\tau)$ as a function of lag time τ computed from the data in (a), including statistical error bars. The superimposed line is a fit to Eq. (3.7).	23

4.1	Overview of holographic particle characterization. (a) Plane-wave illumination is scattered by colloidal particles (red spheres). The field scattered by a particle at \mathbf{r}_p interferes with the plane wave to produce a hologram in the focal plane of a microscope. (b) Features in a digitally recorded hologram are detected with a machine-learning algorithm before being analyzed with light-scattering theory to estimate the particles' physical properties.	29
4.2	Each localization technique provided estimates for the trajectory of a simulated brownian particle. (a) Probability distribution functions for the localization error achieved by (top) heuristic algorithm, (middle) convolutional neural network, and (bottom) cascade classifier. Inset shows expanded view of the subpixel resolution. Vertical dashed line indicates single-pixel precision. (b) Mean-square displacement computed from trajectories obtained with the three detection algorithms. Short-time asymptotes yield dynamical estimates for the localization error. Open circles represent experimental data, as explained in Sec. 4.4.4.	37

4.3 Localization errors as a function of particle radius and refractive index at a height of $z_p = 13.5 \mu\text{m}$ above the focal plane. (a) Cascade classifier. (b) Convolutional neural network. (c) Rate of false positive detections for the cascade classifier. (d) Hologram of a 500 nm-diameter silica sphere that was overlooked by the cascade classifier. This particle was localized to within one pixel by the CNN. (e) Hologram of a 2.4 μm -diameter polystyrene sphere (upper left) interfering with the hologram of a 4.0 μm -diameter TPM sphere located 15 μm above it. Blue dots show feature locations proposed by the heuristic algorithm; Red boxes enclose features detected by the CNN; Dashed black boxes are proposed by the cascade classifier. (f) Hologram of four particles overlaid with regions of interest identified by the CNN. One occluded feature was overlooked by the CNN.	38
4.4 (a) Cascade classifier tracking 2 μm -diameter colloidal spheres diffusing through water in a holographic optical trapping system. Each trace shows 5 seconds of the associated particle's motion. The associated video (Visualization 1) shows the tracking data being used to alternately trap and release the particles. (b) CNN detection of holographic features. The high-contrast feature is created by a 1.5 μm diameter silica sphere. The low-contrast feature represents a coliform bacterium in the dispersion.	44
5.1 The refractive index and diameter of 16 samples of polymerized TPM.	53
5.2 Caption	54

List of Tables

4.1 Analysis times in ms/frame for the heuristic algorithm, the convolutional neural network (CNN) implemented on CPU and GPU, and the cascade classifier implemented on a workstation and on a Raspberry Pi 3 single-board computer.	42
---	----

Chapter 1

Introduction

Chapter 2

Holographic characterization of imperfect colloidal spheres

2.1 Introduction

2.2 Holographic particle characterization

Holographic snapshots of colloidal spheres can be interpreted with the Lorenz-Mie theory of light scattering to measure an individual sphere's three-dimensional position, size and refractive index [1]. When applied to dielectric spheres with near-ideal sphericity and smoothness, this technique yields nanometer-scale precision for the position and radius [1–4] and part-per-thousand precision for the refractive index [1, 5]. Here, we demonstrate that this technique yields similarly precise and meaningful results for imperfect spheres, provided that their deviation from sphericity is not too pronounced.

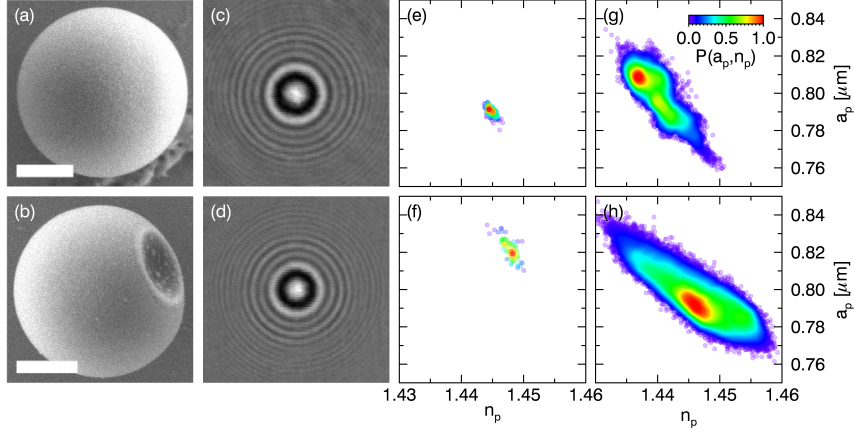


Fig. 2.1: (a) Scanning electron micrograph of a colloidal TPM sphere and (b) a dimpled sphere. Scale bars represent 500 nm. (c) and (d) Corresponding holograms for particles from the samples show in (a) and (b). (e) 5000 measurements of sphere radius and refractive index for a single TPM sphere held in an optical tweezer. Each point represents a single measurement, and is colored according to the relative density of measurements, $P(a_p, n_p)$. (f) equivalent result for a dimpled sphere. (g) 5000 measurements of the radius and refractive index of a freely diffusing sphere. (h) Equivalent result for a dimpled sphere.

Our model system for this work consists of monodisperse colloidal particles synthesized through emulsion polymerization of 3-methacryloxypropyl trimethoxysilane (TPM) [?]. Depending on how they are made, these particles can take the form of spheres, as shown in Fig. 2.1(a), or dimpled spheres, as shown in Fig. 2.1(b), in which both the sphere radius and dimple dimensions are drawn from narrow distributions.

The two types of particles are synthesized through similar pathways. TPM oil, which ordinarily is insoluble in water, undergoes hydrolysis in a basic environment ($\text{pH} > 9$) and becomes water soluble. Solubilized monomers then form

insoluble oligomers, which condense into spherical droplets. Once the droplets are fully grown, they are solidified through free radical polymerization that is initiated by adding 2, 2'-azo-bis-isobutyrylnitrile (AIBN) and heating to 80 °C for 2 h. The particles then are washed and redispersed in deionized water for study.

Homogeneously nucleated TPM droplets form spheres. To synthesize dimpled spheres, we heterogeneously nucleate droplet condensation by adding 0.65 μm -diameter polystyrene spheres to the aqueous phase. These small spheres serve as nucleation sites for TPM condensation and remain embedded in the surface of the resulting droplet to a depth that depends on their wetting characteristics. They remain in place during polymerization, and thus determine the size of the dimple in the final particle. After the TPM is polymerized, the polystyrene spheres are dissolved by transferring the particles into toluene, leaving uniformly sized dimples. For the sample represented by Fig. 2.1(b), the dimple accounts for 5 % of the equivalent sphere's volume, as estimated from scanning electron microscopy images. The completed particles are then transferred back into deionized water for cleaning and study.

Dimpled spheres have immediate applications for lock-and-key colloidal self-assembly [?, ?, ?, ?, ?, ?] and are models for colloidal microcapsules [?], which are widely used in industrial applications, and tend to buckle into dimpled spheres through osmotic stress [?, ?, ?]. They are useful for assessing the limits of holographic characterization because their departure from sphericity is well defined.

We prepared these particles for holographic characterization by dispersing them in water at a volume fraction of 10^{-5} and introduced into a 50 μm -thick gap between a glass microscope slide and a cover slip. The sample is sealed and

mounted on the stage of a custom-built holographic microscope [1, 6], which illuminates it with a collimated laser beam at a vacuum wavelength of $\lambda = 447\text{ nm}$ (Coherent Cube). An illuminated particle scatters some of the laser light to the focal plane of a microscope objective lens (Nikon Plan Apo, $100\times$, numerical aperture 1.4, oil immersion) where it interferes with the unscattered portion of the beam. The interference pattern is relayed by the objective lens and a tube lens to a video camera (NEC TI-324A), which records its intensity at 29.97 frames/s with a calibrated magnification of 135 nm/pixel. The camera's 0.1 ms exposure time is short enough to avoid blurring of the interference pattern due to particle motion [7, 8]. The illumination is linearly polarized with its axis of polarization aligned to within 1° with the \hat{x} axis of the camera.

Each video frame is a hologram of the particles in the $86\text{ }\mu\text{m} \times 65\text{ }\mu\text{m}$ field of view. The images in Fig. 2.1(c) and 2.1(d) are typical holograms of a sphere and a dimpled sphere, respectively. They each subtend 150×150 pixels and are cropped from the camera's 640×480 pixel field of view. Such holograms then can be analyzed [1, 2, 7, 9] with predictions of the Lorenz-Mie theory of light scattering [10, 11] to estimate the particle's radius, a_p and refractive index, n_p . Specifically, we process a recorded image $I(\mathbf{r})$ by subtracting off the camera's dark count, $I_d(\mathbf{r})$ and normalizing by a background image, $I_0(\mathbf{r})$, that is recorded with no particles in the field of view:

$$b(\mathbf{r}) = \frac{I(\mathbf{r}) - I_d(\mathbf{r})}{I_0(\mathbf{r}) - I_d(\mathbf{r})}. \quad (2.1)$$

Assuming that gradients in the amplitude and phase of the illumination are small over the scale of the particle, the normalized hologram of a particle located at \mathbf{r}_p

relative to the center of the microscope's focal plane may be modeled as [1,4]

$$b(\mathbf{r}) = |\hat{x} + e^{-ikz_p} \mathbf{f}_s(k(\mathbf{r} - \mathbf{r}_p))|^2, \quad (2.2)$$

where $k = 2\pi n_m / \lambda$ is the wave number of the light in a medium of refractive index n_m , and where $\mathbf{f}_s(k\mathbf{r})$ describes how the particle scatters \hat{x} -polarized light.

If the particle may be modeled as an ideal isotropic sphere, then $\mathbf{f}_s(k\mathbf{r})$ is the Lorenz-Mie scattering function [10,11], which is parameterized by the particle's radius and refractive index. Fitting Eq. (2.2) to a measured hologram therefore yields the particle's three-dimensional position \mathbf{r}_p , its radius a_p and its refractive index n_p . Previous studies on model colloidal spheres have confirmed that these fits converge reliably for micrometer-scale spheres, and yield the radius with a precision better than 5 nanometers [1,3,4] and the refractive index to within 3 parts per thousand [3,5]. The data in Fig. 2.1(e) show results obtained for a typical TPM sphere localized in an optical trap that was projected through the microscope's objective lens using the holographic optical trapping technique [?,12]. The spread in values is comparable to the numerically estimated uncertainty in the individual fits, $a_p = 0.790 \pm 0.003 \mu\text{m}$ and $n_p = 1.445 \pm 0.001$, suggesting both that the imaging model is appropriate, and also that the signal-to-noise ratio estimated by the median-absolute-deviation (MAD) metric is reasonable. This sphere's holographically measured radius is consistent with the mean value, $0.76 \pm 0.06 \mu\text{m}$, obtained through SEM observations on the same batch of spheres. The polymerized particles' refractive index is larger than that of monomeric TPM oil, 1.431 at the imaging wavelength.

The scattering function for an aspherical object, such as a dimpled sphere,

depends on the object’s detailed shape and orientation [11]. Analytical results are available for just a few special cases. For more general cases, numerical methods are required, such as the discrete dipole approximation (DDA) [13]. Even with highly optimized implementations [?], however, such approaches are computationally intensive [?, ?, 14]. If an object’s departure from sphericity is small enough, and if the influence of the non-ideality on the recorded hologram is sufficiently well localized within the recorded image, Lorenz-Mie analysis may still yield useful results for the particle’s size and refractive index without incurring this cost.

Figure 2.1(f) shows results obtained by fitting the ideal-case model to holograms of an optically trapped dimpled sphere. The radius estimated by straightforward Lorenz-Mie analysis of 60 such holograms is $0.821 \pm 0.006 \mu\text{m}$. The corresponding estimate for the refractive index, 1.448 ± 0.001 is remarkably similar to the value obtained for the ideal spheres. In both cases, the distribution of values extracted from nonlinear least-squares fits to Eq. (2.2) is consistent with single-fit error estimates. This agreement suggests that the ideal model can yield quantitative results for the characteristics of dimpled spheres, without incurring the costs of more realistic modeling.

SEM analysis suggests that the sample-averaged radius of the dimpled spheres is $0.75 \pm 0.05 \mu\text{m}$, which is slightly smaller than the result obtained holographically. Similar discrepancies have been noted in previous studies [?, ?], and reasonably may be explained by changes induced by preparing the spheres for SEM observation.

The extent to which a dimpled sphere’s hologram may be described with an ideal sphere’s scattering function depends on the dimple’s orientation. Opti-

cally trapping a dimpled sphere constrains its rotations as well as its translations, fixing the dimple’s axis in the transverse plane. When released from its trap, the dimpled sphere rotates freely in three dimensions, with consequences for holographic characterization. Figure 2.1(g) shows the distribution of characteristics obtained over the course of 10 min for a freely diffusing sphere. The mean radius and refractive index obtained for this particle are $0.80 \pm 0.01 \mu\text{m}$ and 1.440 ± 0.003 , respectively. Additional uncertainty in the particle’s radius and refractive index reflects uncorrected interference artifacts in the recorded hologram due to defects in illumination [4]. The corresponding distribution for the freely diffusing dimpled sphere is broadened still further, and displays a strong anticorrelation between radius and refractive index. The peak of this distribution remains at the trapped-particle values, $a_p = 0.80 \pm 0.01 \mu\text{m}$ and $n_p = 1.447 \pm 0.005$, presumably because the randomly oriented particle is more likely to have its dimple transverse to the optical axis than facing it.

Having the dimple pointing sideways is beneficial for holographic characterization. In this orientation, the dimple’s contribution to the scattering pattern is asymmetric, and thus minimally influences the fit to the largely symmetric model. It plays a role comparable to uncorrected background artifacts, reducing the precision, but not seriously affecting the mean values. When the dimple is directed along the axis, however, distortions to the scattering pattern are symmetric about the axis and thus affect the fits more strongly.

The success of an idealized model for describing light scattering by a dimpled sphere may be explained at least heuristically by treating the dimple as a volume of the sphere whose scattering is phase-shifted by 180° . The scattering

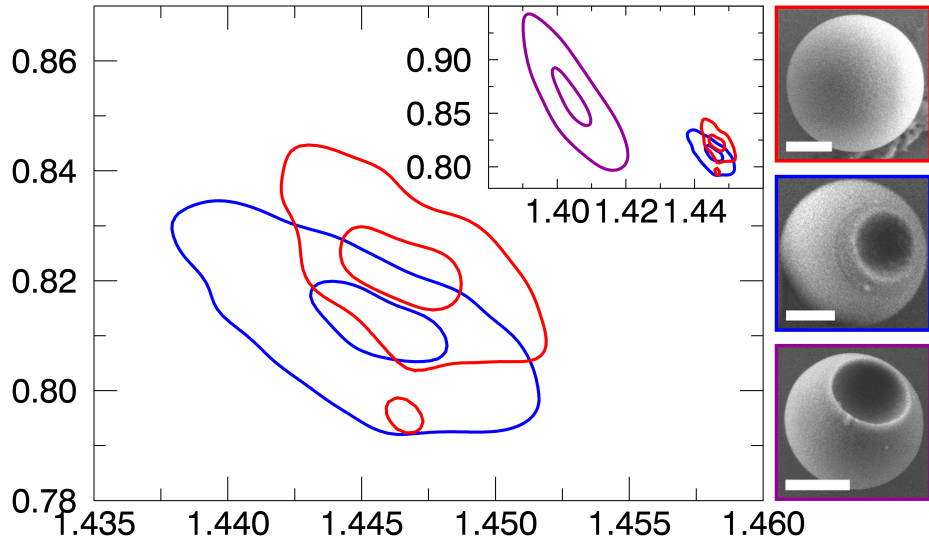


Fig. 2.2: Level sets of the holographically measured distributions of particle properties for TPM spheres (red), dimpled spheres with small dimples (blue) and large dimples (purple). The presence of a small dimple has no significant influence on holographic characterization results. Larger dimples cause systematic errors. SEM images show typical representatives of each sample, with scale bars denoting 500 nm.

amplitudes for the sphere as a whole and for the dimple scale roughly as their respective volumes. If the dimple’s volume is only a small fraction of the sphere’s, and if, furthermore, the dimple’s contribution is asymmetric, the perturbation should be negligible.

We applied the same technique to characterizing the distribution of properties in monodisperse samples of TPM spheres and TPM dimpled spheres. For these measurements, dispersions of particles at a volume fraction of 10^{-4} were streamed down a channel by a pressure driven flow with a peak speed of $100 \mu\text{m/s}$. This is fast enough to acquire holograms of 5000 spheres in 10 min, but not so

fast as to incur artifacts due to motion-induced blurring [7, 8]. Results plotted in Fig. 2.2 for TPM spheres reveal a reasonably symmetric distribution of particle sizes and refractive indexes peaked at $0.82 \pm 0.02 \mu\text{m}$ and 1.446 ± 0.006 , respectively. These values are consistent both with the single-sphere measurements reported in Fig. 2.1. The corresponding distributions for dimpled spheres plotted in Fig. 2.2 become increasingly broad and asymmetric as the relative size of the dimple increases. Particles with 5 % dimple volumes yield a mean refractive index, 1.444 ± 0.006 , consistent with the ideal spheres' value. The mean radius, $0.81 \pm 0.02 \mu\text{m}$, is consistent with the single-sphere result reported in Fig. 2.1(h). Increasing the dimple volume to 10 % leads to substantial deviations, with a mean refractive index of 1.42 ± 0.03 . Some variability can be attributed to the dimpled spheres' random orientation in the channel.

To assess the extent of the distortions that can be handled with the idealized model for holographic characterization, we apply the discrete-dipole approximation [?, ?, ?, 13, 14] to compute holograms of dimpled spheres, and then analyze the resulting synthetic data with the same software used to analyze experimental data. The discrete-dipole approximation treats an object as a three-dimensional arrangement of independent microscopic dipole scatterers, each of which is illuminated by the incident beam and also by the first-order scattering of its neighbors ¹. The superposition of scattered waves yields an estimate for $\mathbf{f}_s(k\mathbf{r})$, which is used to synthesize a hologram. Dimpled spheres are modeled as the superposition of two spheres separated by a center-to-center distance d , one of radius a_p and refractive

¹The ADDA implementation of the discrete-dipole approximation [?] used for this study discretizes the particle volume on a three-dimensional square grid with an effective lattice constant roughly one-tenth the wavelength of light in the material. Typical numbers of dipoles range from 100 for the smallest particles considered to 18 000 for the largest.

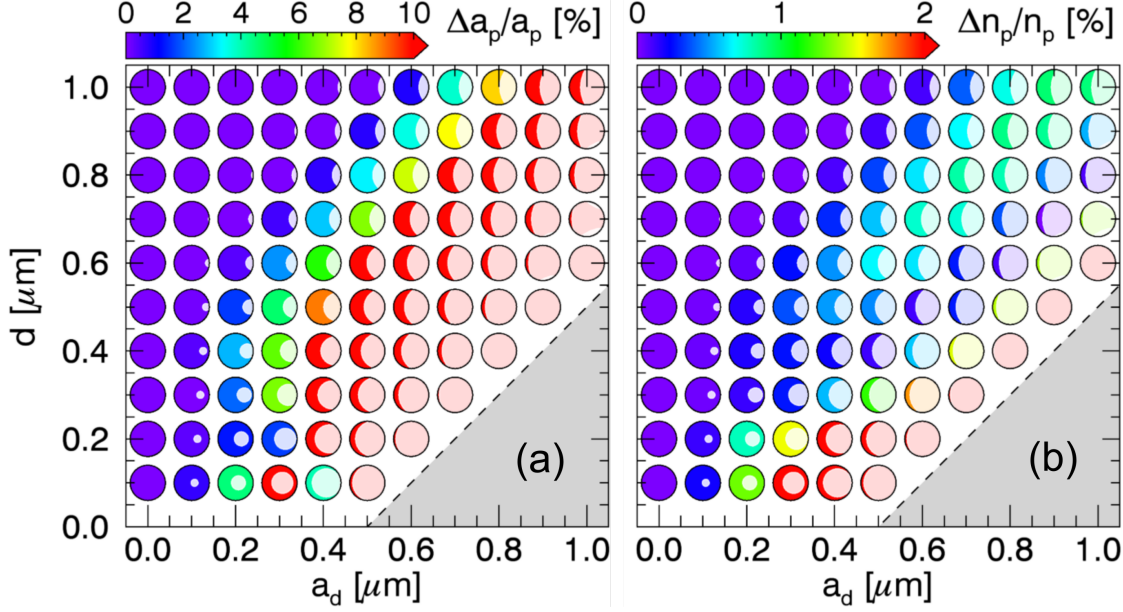


Fig. 2.3: Holographic characterization of dimpled TPM spheres with radius $a_p = 0.5 \mu\text{m}$ as a function of dimple radius a_d and center-to-center distance, d . (a) Relative error in holographically estimated radius. (b) Relative error in refractive index. Plot symbols indicate shape of dimpled spheres.

index n_p , and the other of radius a_d and the refractive index of the medium.

Analyzing DDA-generated holograms of perfect spheres yields excellent agreement with input parameters for sphere radii up to $a_p \leq 0.5 \mu\text{m}$. Scattering by larger spheres requires proper treatment of higher-order scattering, and is not supported by the ADDA implementation of the DDA algorithm that we adopted [?, ?]. Limiting the analysis to parameters within the spherical particle's domain of applicability, we assessed discrepancies between input parameters and values obtained by fitting the resulting holograms with the scattering function for ideal spheres.

Figure 2.3 summarizes the performance of Lorenz-Mie analysis for char-

acterizing spheres bearing a single dimple. The colors of the plot symbols in Fig. 2.3(a) represent the relative error in the radius obtained by applying the Lorenz-Mie analysis to the computed hologram of a dimpled sphere. The plot symbols' shapes correspond to the dimpled particles' medial profile for each value of a_p and d . Figure 2.3(b) shows the corresponding results for the refractive index. Deviations become larger for spheres distorted by larger dimples, particularly if those dimples are aligned with the optical axis. This leaves a substantial domain of applicability within which computationally efficient implementations of hologram analysis can be used to measure the properties of this class of imperfect spheres. As a rule of thumb, near-ideal results can be obtained for dimples that take up no more than 5 % of a sphere's volume.

The same approach also should be useful for characterizing colloidal particles with multiple dimples, so-called colloidal golf balls [?], and for colloidal snowmen [?] with small protrusions instead of dimples. Simulations with up to 10 equally-sized dimples distributed uniformly across the sphere's surface yield values for a_p and n_p within 1 % of the ideal values for total dimple volumes less than 5 % of the sphere's volume. The influence of orientation becomes less pronounced as the number of dimples increases. Removing a larger percentage of the volume yields disproportionately worse results.

The success of holographic particle characterization for analyzing holograms of imperfect spheres helps to explain the technique's previously documented success with real-world samples. This study suggests that small amounts of surface roughness have little influence on the results obtained by fitting to the theory for light scattering by ideal spheres. These observations therefore broaden the domain

of applicability of holographic characterization.

This work was supported primarily by the MRSEC program of the National Science Foundation through Grant Number DMR-1420073, in part by the NSF through Grant Number DMR-1305875, in part by the U.S. Army Research Office under Grant Award No. W911NF-10-1-0518 and in part by a grant from Procter & Gamble. The holographic characterization instrument was developed under support of the MRI program of the NSF through Grant Number DMR-0922680. The scanning electron microscope was purchased with financial support from the MRI program of the NSF under Award DMR-0923251.

Chapter 3

Machine-learning approach to holographic particle characterization

3.1 Introduction

Holograms of colloidal spheres obtained with holographic video microscopy [6, 15] can be interpreted with predictions of the Lorenz-Mie theory of light scattering [10] to track each particle in three dimensions, and to measure its size and refractive index [1]. State-of-the-art implementations [?, ?, ?, 1] can locate a sphere and resolve its radius both to within a few nanometers, and can determine its refractive index to within a part per thousand [4, 5, 7]. The cost of this powerful technique is the computational burden of fitting each hologram pixel-by-pixel to theoretical predictions [1, 2]. Here, we demonstrate that techniques of machine

learning can reduce the processing time by a factor of a thousand, yielding real-time performance.

Our approach to fast holographic characterization, depicted schematically in Fig. 3.1, employs the support vector machine (SVM) algorithm [?] to compare experimental measurements with pre-computed predictions of the Lorenz-Mie theory [1, 9, 10]. Whereas nonlinear fitting typically requires more than a second on a 1 Gflop computer, a trained SVM can estimate the size, refractive index or axial position of a micrometer-scale sphere in under a millisecond on the same hardware.

3.2 Fast Holographic Characterization with Machine Learning

The in-line holographic microscope used for these studies [1, 4, 6] illuminates the sample with a linearly polarized collimated laser beam (Coherent Cube, 20 mW) at a vacuum wavelength of $\lambda = 447 \text{ nm}$. The fluence of the 3 mm-diameter beam is comparable to that of a conventional microscope illuminator. Optical forces and light-induced heating therefore are negligible. Light scattered by a sphere propagates to the focal plane of a custom-built video microscope [4] where it interferes with the undiffracted portion of the original beam. The microscope magnifies this interference pattern onto the detector of a greyscale video camera (NEC TI 324AII), which records its intensity with a system magnification of 135 nm/pixel. Each snapshot in the video stream constitutes a hologram of the particles in the channel.

The electric field of the incident beam at position \mathbf{r} in the focal plane may

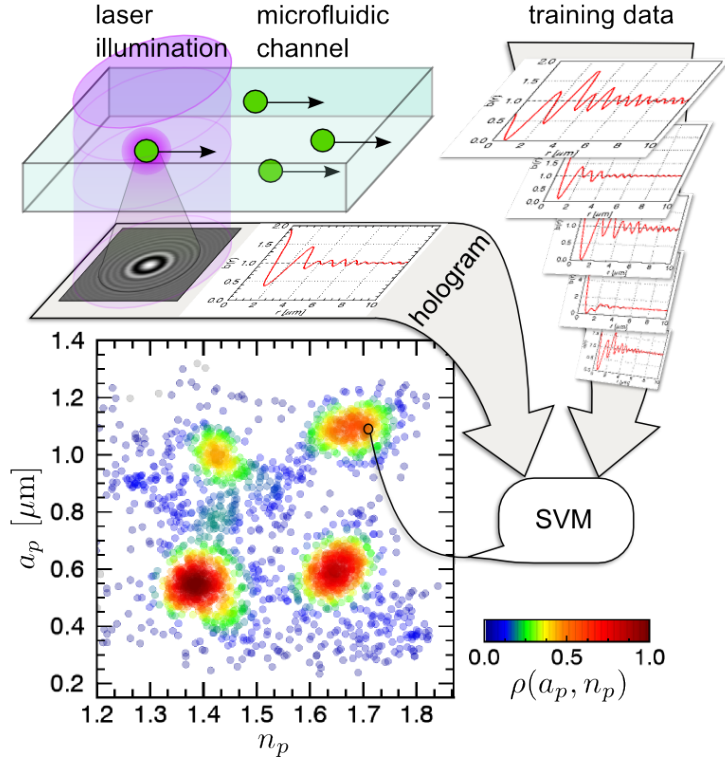


Fig. 3.1: Colloidal characterization by holographic microscopy and machine learning. Colloidal spheres flowing down a microfluidic sample scatter light from a collimated laser beam to form an in-line hologram. Features in the beam are identified, and their radial profiles presented to support vector machines (SVMs) that compare them with a library of training data to estimate each spheres' radius a_p and refractive index n_p . The scatter plot shows results for 2,500 spheres drawn at random from a mixture of four different types of spheres. Each point is colored by the local density of data points, $\rho(a_p, n_p)$.

be modeled as a plane wave with spatial dependence

$$\mathbf{E}_0(\mathbf{r}) = u_0(\mathbf{r}) e^{i\varphi_0(\mathbf{r})} e^{ikz} \hat{x}, \quad (3.1)$$

where $k = 2\pi n_m / \lambda$ is the wavenumber in a medium of refractive index n_m , and where $u_0(\mathbf{r})$ and $\varphi_0(\mathbf{r})$ account for small variations in the beam's amplitude and phase profiles, respectively.

A particle located at \mathbf{r}_p relative to the center of the focal plane scatters the incident illumination, $\mathbf{E}_0(\mathbf{r}_p)$, to the focal plane as

$$\mathbf{E}_s(\mathbf{r}) = E_0(\mathbf{r}_p) \mathbf{f}_s(k(\mathbf{r} - \mathbf{r}_p) | a_p, n_p), \quad (3.2)$$

where $\mathbf{f}_s(kr | a_p, n_p)$ is the Lorenz-Mie scattering function [10] that describes how a sphere of radius a_p and refractive index n_p scatters an \hat{x} -polarized plane wave. The measured intensity then may be modeled as

$$I(\mathbf{r}) = |\mathbf{E}_0(\mathbf{r}) + \mathbf{E}_s(\mathbf{r})|^2. \quad (3.3)$$

Normalizing the recorded hologram by $I_0(\mathbf{r}) = |\mathbf{E}_0(\mathbf{r})|^2 = u_0^2(\mathbf{r})$ suppresses spurious structure in the illumination and yields a functional form for the normalized hologram [1, 4],

$$b(\mathbf{r}) = \frac{I(\mathbf{r})}{I_0(\mathbf{r})} \approx |\hat{x} + e^{-ikz_p} \mathbf{f}_s(k(\mathbf{r} - \mathbf{r}_p) | a_p, n_p)|^2, \quad (3.4)$$

that can be calculated with standard software packages [?].

Previous implementations of Lorenz-Mie microscopy [1] fit Eq. (3.4) to

measured holograms using a_p , n_p and \mathbf{r}_p as adjustable parameters. These fits are exquisitely sensitive to errors in the particle's in-plane position, and so must be performed over the entire two-dimensional intensity distribution [1]. Here, we instead use Eq. (3.4) to train support vector machines, which then are able to estimate a_p , n_p and z_p from a hologram's one-dimensional radial profile. We obtain these profiles from measured holograms by averaging around centers of rotational symmetry [9] with single-pixel resolution, yielding 100-point data vectors. The microscope's focal plane is adjusted so that the interference fringes in a typical sphere's hologram extend to roughly this scale. Averaging over angles to obtain a radial profile reduces the dimensionality of the analysis problem and accounts in part for our method's computational efficiency.

Our SVMs are implemented with `scikit-learn`, an open-source machine learning software package [?] that builds upon the `libsvm` library of Support Vector Machine algorithms [?, ?]. Each SVM computes one output parameter from an input vector consisting of a radial profile, $b(r)$, that has been digitized into 100 single-pixel bins. Characterizing and tracking a colloidal particle therefore requires three SVMs, one for each of a_p , n_p and z_p . Figure 3.1 schematically represents this process for estimating a_p and n_p .

An SVM computes its output by comparing $b(r)$ with sets of training data, $b_n(r)$, that are obtained from Eq. (3.4) over a range of values of a_p , n_p and z_p . Each training set constitutes one support vector in the space spanned by these parameters. To facilitate these comparisons, we construct SVMs with radial basis functions [?],

$$k_n(b) = \exp\left(-\gamma \int |b_n(r) - b(r)|^2 dr\right), \quad (3.5)$$

that quantify the similarity of the experimental input with the n -th support vector. The sensitivity of this comparison is set by γ , with larger values favoring more precise results at the cost of requiring more support vectors to span the parameter space. Given a value of γ , the training process determines a set of weights ω_n and an offset s_0 such that the weighted sum,

$$\tilde{s}(b) = \sum_n \omega_n k_n(b) + s_0, \quad (3.6)$$

constitutes an estimate for the parameter, $s(b)$, that characterizes the input data vector, $b(r)$. In general, errors in $\tilde{s}(b)$ depend smoothly on γ [?].

To prevent overfitting, the weights ω_n are constrained to have magnitudes less than a maximum value, which conventionally is denoted by C [?]. Optimizing an SVM with larger values of C improves its ability to recognize its training data, but renders it less able to interpolate smoothly between its support vectors when presented with novel or noisy inputs. Some candidate support vectors may be assigned small weighting factors in optimizing $\tilde{s}(b)$ over a corpus of training data; these are automatically eliminated from the SVM [?]. The choice of γ and C thus determines which support vectors are included in the SVM, and their relative importance for computing the output. Because this process is nonlinear, optimal values are obtained by exhaustive search over the range $0.1 \leq \gamma \leq 10$ and $0.1 \leq C \leq 1,000$. Statistically indistinguishable results are obtained in the present application for values of γ and C that vary from their optimal values by up to fifty percent.

We trained SVMs with a 5,000-member training set of radial profiles, $b_n(r)$, computed with Eq. (3.4) using the Lorenz-Mie theory. Parameters for these

computed profiles were evenly distributed over a volume in the three-dimensional space spanned by $13.5 \mu\text{m} \leq z_p \leq 75 \mu\text{m}$, $0.4 \mu\text{m} \leq a_p \leq 1.75 \mu\text{m}$, and $1.4 \leq n_p \leq 1.8$ at a resolution of $1.35 \mu\text{m}$ in z_p , $0.1 \mu\text{m}$ in a_p and 0.1 in n_p . Training time increases dramatically with the number of training sets, and also with larger values of C and γ . Once trained, however, an SVM translates input data vectors into output parameter estimates extremely rapidly.

The quality of a trained SVM can be assessed by presenting it with independently computed cross-validation data. Optimal values for C and γ minimize differences between estimated parameters and the inputs. Using a 500-member cross-validation set, we obtained best performance for estimating z_p with $C = 100$ and $\gamma = 1$, best performance for n_p with $C = 10$ and $\gamma = 0.5$, and best performance for a_p with $C = 10$ and $\gamma = 0.6$.

Sampling the entire parameter space accessible to holographic characterization with resolution comparable to the precision realized with nonlinear fits [1] would require more than 10^{10} training sets. If, however, the system of interest is characterized by a more modest range of parameters, then results from an initial SVM analysis can be used to generate a comparatively small set of training data spanning the relevant range. This specialized training proceeds rapidly and yields substantial improvements in precision.

3.3 Characterization of Colloidal Mixtures

The data plotted in Fig. 3.1 are SVM estimates for the radii and refractive indexes of 2,500 colloidal spheres flowing down a $20 \mu\text{m}$ -deep microfluidic channel

formed by bonding the edges of a glass microscope cover slip to the surface of a glass microscope slide. The peak flow speed of 1 mm/s transports a sphere across the field of view in no fewer than two video frames, ensuring that every particle in the flow has a chance to be analyzed. Anisotropic blurring due to a sphere’s 100 nm motion during the camera’s 0.1 ms exposure time suppresses contrast along the direction of motion, but does not appreciably influence the azimuthal average, $b(r)$ [8]. Spurious results arising when multiple spheres’ interference patterns overlap contribute outliers to the observed distribution of particle sizes and refractive indexes. Such artifacts are minimized by diluting the sample to a volume fraction less than 10^{-3} so that no more than three particles are present in any frame.

The sample was prepared by dispersing roughly equal proportions of four types of colloidal spheres in water: 1 μm -diameter and 2 μm -diameter spheres made of polystyrene (Thermoscientific Catalog No. 5100A and Bangs Laboratories Catalog No. SS04N, respectively) and silica (Duke Standards Catalog Nos. 8100 and 4202A, respectively). Each of these four populations is monodisperse, with a standard deviation in the radius of less than 5%. This four-component mixture was flowed through the observation volume during a 12 min interval, and analyzed particle-by-particle. Each data point in Fig. 3.1 corresponds to an individual sphere, and is colored by the local density of measurements.

SVM-mediated holographic characterization clearly identifies the four populations of particles and provides estimates for their relative abundances. The mode values of the refractive indexes, $n_p \approx 1.4$ and 1.6 are consistent with values for silica and polystyrene, respectively. Values for the radii, $a_p \approx 0.5 \mu\text{m}$ and 1 μm are consistent with manufacturers’ specifications. Characterizing multicom-

ponent dispersions is a unique capability of holographic particle analysis, and can be performed with SVMs as fast as particles' holograms can be acquired. This performance is all the more noteworthy because the distribution of particle properties is built up one particle at a time and so does not rely on *a priori* assumptions.

Neither the instrument nor the analytical technique requires extensive calibration. The wavelength of the laser and the effective magnification can be calibrated once and used for all samples. The refractive index of the medium is the only free parameter, and often can be obtained separately. These parameters are used to train the SVMs in advance, after which they can be used to analyze arbitrary samples dispersed in the medium.

3.4 Tracking and Assessment of Precision

Tracking a single colloidal sphere as it sediments and diffuses provides insights into the precision and accuracy of SVM-mediated holographic characterization. The data in Fig. 3.2 were obtained with a 1.59 μm -diameter polystyrene sphere (Duke Scientific, catalog 4016A) diffusing as it sedimented through deionized water near the midplane of a 120 μm -deep channel. Figure 3.2(a) shows the time-resolved trajectory, $z_p(t)$, obtained from a sequence of 4,500 video frames recorded at 29.97 frames/s using iterative SVM training.

Because polystyrene is roughly 5 percent more dense than water, the sphere sediments more than 10 μm over the course of the experiment. The insets to Fig. 3.2(a) show how markedly the hologram's appearance changes from the beginning of the trajectory to the end. Despite these changes, the SVMs' es-

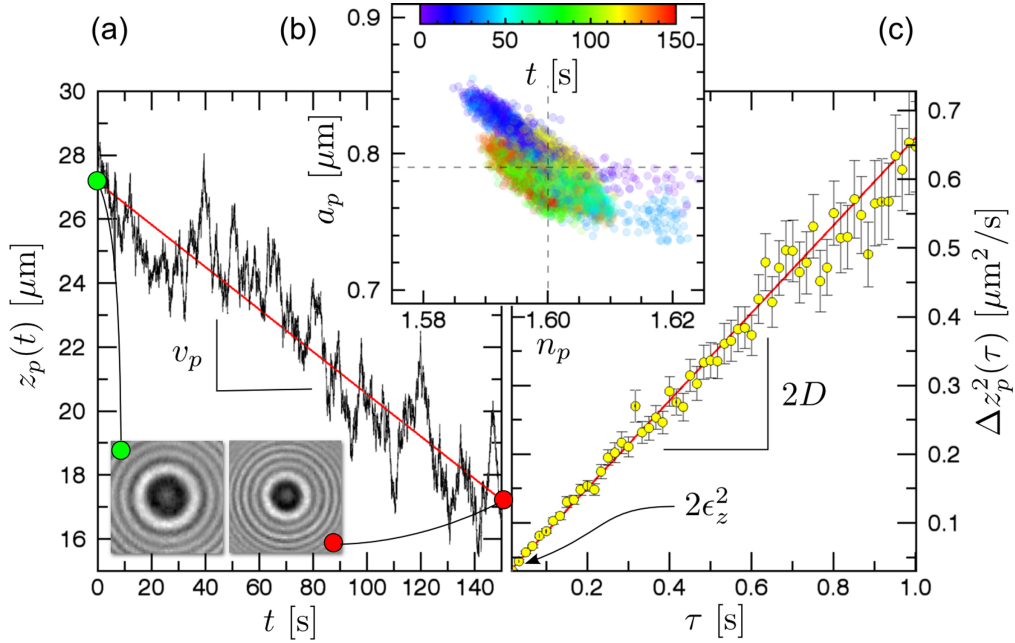


Fig. 3.2: Tracking and characterizing a single colloidal sphere. (a) The estimated axial position $z_p(t)$ relative to the focal plane of the microscope of a single polystyrene sphere sedimenting through water as it diffuses. The line is a least-squares fit. Insets show the sphere's hologram at the beginning and end of the trajectory. (b) The radius a_p and refractive index n_p estimated from each hologram in the same sequence, colored by time. Each dot corresponds to values obtained from a single hologram. (c) The mean-squared displacement, $\Delta z_p^2(\tau)$ as a function of lag time τ computed from the data in (a), including statistical error bars. The superimposed line is a fit to Eq. (3.7).

timates for the radius and refractive index plotted in Fig. 3.2(b) remain clustered around the mean values $a_p = 0.79 \pm 0.02 \mu\text{m}$ and $n_p = 1.600 \pm 0.006$.

Uncertainties in estimated parameters are computed as standard deviations of the distribution of results plotted in Fig. 3.2(b). These should be interpreted with care because errors in SVM estimates need not be independent or normally distributed. Data points in Fig. 3.2(b) cluster around different values as the particle descends, which suggests that different support vectors dominate the estimates for a_p and n_p when the sphere is at different axial positions. Systematic errors in the individual parameters therefore may vary with changes in any of the parameters' values. Even so, the averages of the SVM estimates are consistent with the manufacturer's specifications, and differ only slightly from those obtained with a full Lorenz-Mie analysis of the same data set [4], which yields $a_p = 0.805 \pm 0.001 \mu\text{m}$ and $n_p = 1.5730 \pm 0.0006$. Nonlinear fitting offers ten times better precision and accuracy [4]. SVM analysis is a thousand times faster.

The mean sedimentation speed, $v_p = 66 \pm 1 \text{ nm/s}$, estimated from the slope of $z_p(t)$ is somewhat smaller than the value measured with fits to the Lorenz-Mie theory [4] of $75 \pm 1 \text{ nm/s}$. This discrepancy further suggests that the SVM estimate for a parameter's value may depend on the value itself. If we nevertheless assume that errors in z_p are normally distributed with a root-mean-square value ϵ_z , then the diffusing particle's mean-squared displacement should evolve over time interval τ as

$$\Delta z_p^2(\tau) \equiv \langle [z_p(t + \tau) - z_p(t)]^2 \rangle_t = 2D\tau + v_p^2\tau^2 + 2\epsilon_z^2, \quad (3.7)$$

where $D = k_B T / (6\pi\eta a_p)$ is the Stokes-Einstein value for the particle's diffusion

coefficient. The data in Fig. 3.2(c) yield $D = 0.319 \pm 0.004 \mu\text{m}^2/\text{s}$, which is slightly larger than the value of $0.292 \pm 0.004 \mu\text{m}^2/\text{s}$ obtained with the full Lorenz-Mie analysis [4]. The best-fit tracking error, $\epsilon_z = 107 \pm 2 \text{ nm}$, exceeds the Lorenz-Mie bound by an order of magnitude [4].

3.5 Conclusions

The results presented here are typical of the performance of SVMs for characterizing and tracking colloidal spheres. of a wide variety of compositions and sizes over a large axial range. The speed and precision of SVM characterization is ideal for monitoring, feedback control and quality assurance in any industrial process involving colloidal spheres. In applications where the greatest precision is required, parameters estimated with SVMs can be used to initialize nonlinear least-squares fits. Starting from such reasonable estimates speeds convergence and reduces the likelihood of failed fits. Being able to resolve multimodal distributions by quickly amassing single-particle measurements avoids ambiguities inherent in population-averaging methods such as dynamic light scattering. Extracting the refractive index as well as the size offers insights into sample composition that otherwise would not be available. SVM-accelerated tracking can be used for real-time three-dimensional particle-tracking velocimetry [7]. For applications such as microrefractometry [5], the medium's refractive index, n_m , can be estimated instead of the particle's.

This combination of capabilities enables new applications. For example, the distribution of properties in colloidal mixtures could serve as fingerprints for

complex fluid systems, with the sizes, refractive indexes and relative abundances encoding information that can be accessed with SVM-mediated holographic characterization.

Such applications can be realized with comparatively simple instruments [4] conveying image data to low-power computers. Although training SVMs can be computationally intensive, the data comprising a set of trained SVMs occupies less than 100 Mbyte. Pre-computed SVMs therefore can be archived and rapidly retrieved when needed. This approach lends itself to implementation on embedded computers for integration into low-cost analytical instruments.

Other machine-learning techniques also might be effective for analyzing holograms of colloidal particles. Artificial neural networks, for instance, can be trained in the same manner as the present SVM implementation to interpret radial profiles of experimental holograms. SVMs have the advantage that their training process proceeds deterministically, and therefore tends to be faster. Once successfully trained, however, artificial neural networks are generally more computationally efficient. Regardless of implementation, the present results demonstrate that machine-learning methods facilitate fast and precise measurements of colloidal properties.

Chapter 4

Machine-learning techniques for fast and accurate feature localization in holographic images

4.1 Introduction: Holographic Particle Charac- terization

Holographic particle characterization [1] uses quantitative analysis of holographic video microscopy images to measure the size, shape, and composition of individual colloidal particles, in addition to their three-dimensional positions. When applied to a stream of dispersed particles, holographic characterization measurements provide insights into the joint distribution of particle size and composition that cannot be obtained in any other way. This technique has been demonstrated

on both homogeneous and heterogeneous [?, 16] dispersions of colloidal spheres, and has been extended to work for colloidal clusters [?, 14, 17], and aggregates [18, 19], as well as colloidal rods [20] and other aspherical particles [?, 21]. Applications include monitoring protein aggregation in biopharmaceuticals [18], detecting agglomeration in semiconductor polishing slurries [?], gauging the progress of colloidal synthesis reactions [22, 23], performing microrheology [?], microrefractometry [5], and microporosimetry [24] measurements, assessing the quality of dairy products [25], and monitoring contaminants in wastewater [?].

The critical first step in holographic particle characterization is to detect features of interest within a recorded video frame, and to localize them well enough to enable subsequent analysis [7, 9, 16, 26]. False positive and negative detections clearly are undesirable. Poor localization slows downstream analysis [9, 16] and can prevent fitting algorithms from converging to reasonable results. Here, we demonstrate that machine-learning algorithms can meet the need for reliable feature detection and precise object localization in holographic video microscopy. This complements the previously reported [16] use of machine-learning regression to estimate characteristics such as particle size from holographic features that already have been detected, localized and isolated by other means. With appropriate training, machine-learning algorithms surpass standard image-analysis techniques in their ability to cope with common image defects such as overlapping features. They also operate significantly faster, thereby enabling applications that benefit from real-time performance on low-cost hardware.

4.2 Detecting and Localizing Holographic Features

Figure 4.1 illustrates the challenge of recognizing features in holograms. Light scattered by a particle spreads as it propagates to the focal plane of a conventional microscope. There, it interferes with the remainder of the illuminating beam to create a pattern of concentric interference fringes. The microscope magnifies this interference pattern and projects it onto the detector of a video camera. The intensity variations associated with a single colloidal particle typically span many pixels in a recorded image and display rich internal structure. Their scale and complexity render such features difficult to recognize by conventional particle-tracking

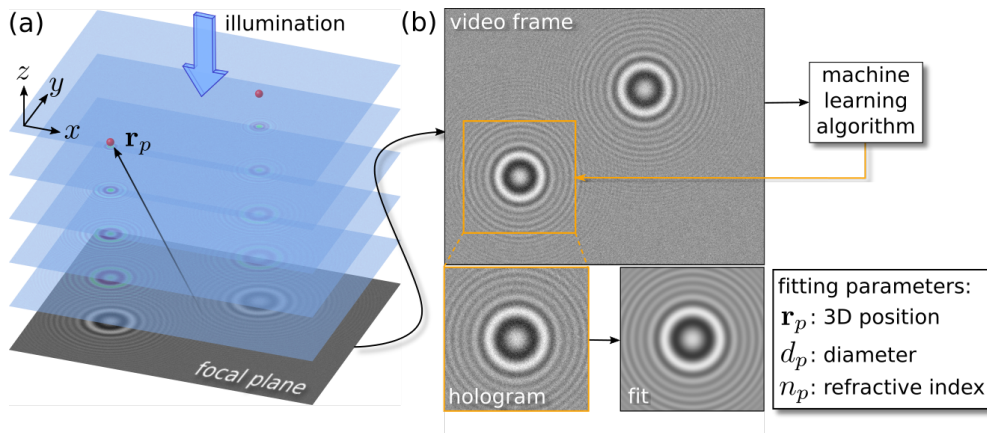


Fig. 4.1: Overview of holographic particle characterization. (a) Plane-wave illumination is scattered by colloidal particles (red spheres). The field scattered by a particle at \mathbf{r}_p interferes with the plane wave to produce a hologram in the focal plane of a microscope. (b) Features in a digitally recorded hologram are detected with a machine-learning algorithm before being analyzed with light-scattering theory to estimate the particles' physical properties.

techniques.

4.2.1 Heuristic Algorithms

One practical method for detecting holographic features and locating their centers involves transforming extended interference patterns into compact peaks [7, 9], and then locating the peaks with standard centroid detectors [?, 26]. Successful implementations of this two-step approach have been based on voting algorithms such as the circular Hough transform [?, ?, 7] and the orientation alignment transform [9]. Both of these feature-coalescence algorithms rely on the radial symmetry of typical single-particle holograms' symmetry without reference to the underlying image-formation mechanism. For an image of N pixels on a side, voting algorithms have a computational complexity of $\mathcal{O}N^3 \log N$ [?] whereas the convolution-based orientation alignment transform runs in $\mathcal{O}N^2 \log N$ operations [7]. For this reason, we transform holograms with the orientation alignment transform to assess the performance of heuristic algorithms, using an open-source implementation described in [7].

The peaks created by feature coalescence can be detected and their centroids localized as local maxima in the transformed images. When presented with holograms of well-separated colloidal spheres, heuristic algorithms provide sub-pixel precision for particle localization [7, 9]. This easily meets the need to localize features for subsequent analysis. We use the open-source TrackPy implementation [?] of the Crocker-Grier algorithm [26].

Detecting and localizing local maxima can be very efficient if the peaks have well-defined widths, heights and separations [?, 26]. Transformed holograms of

colloidal particles, however, can have widely varying contrasts and extents depending on the particles' properties and heights above the focal plane. Thresholds for feature detection and localization therefore must be assessed from the transformed images themselves. This can create a bottleneck for heuristic feature detection and localization.

4.2.2 Machine-Learning Algorithms

Machine-learning techniques can reduce the computational burden of detecting and localizing features of interest in holographic microscopy images, and also prove to be more robust against false positive and negative feature detections. We have implemented two such approaches: a cascade of boosted classifiers based on Haar-like wavelets, and a deep convolutional neural network (CNN). Both approaches yield estimates for the in-plane coordinates, (x_p, y_p) , for every particle in the field of view, as well as the extent of the region of interest encompassing the scattering pattern. The box superimposed on the two-particle hologram in Fig. 4.1(b) represents a region of interest centered on one of the particles that was computed by a CNN.

Cascade classifiers and convolutional neural networks both work by convolving holograms with small arrays and interpreting the results. They thus require $\mathcal{O}N^2$ operations, which gives them the potential to run significantly more quickly than heuristic algorithms, particularly for larger images. Each has particular strengths for particle localization in holographic microscopy images.

Cascade classifiers were originally developed for detecting faces in photographs [?]. They work by convolving an image with a sequence of selected

wavelets, each of which is considered to be a “weak classifier” for objects of interest. An above-threshold response from a linear combination of such weak classifiers signifies the presence of a feature of interest centered at the point of strongest response. Regions containing such above-threshold responses are analyzed with the weak classifiers at the next step of the cascade. Any regions that remain after analysis by the full cascade are considered to be features. The analysis is performed at a sequence of resolutions to capture features at different scales. Haar wavelets are particularly attractive for this application because they are implemented in integer arithmetic with highly efficient algorithms. The training process determines which Haar wavelets constitute useful weak classifiers at each level of the cascade, and which combinations best serve as strong classifiers for features of interest. Training also optimizes the number of stages of increasingly fine resolution required to detect features reliably and to localize them with a requested precision. This approach has been adapted for a wide range of object recognition and image segmentation tasks [?]. Our application of this technique to holographic feature localization is based on an open-source implementation of Haar cascade classifiers made available by the OpenCV project [?]. This cascade classifier can be trained to recognize non-standard features of interest, such as holograms of colloidal particles. For each such feature in a hologram, it yields a candidate set of rectangular regions of interest that may include multiple estimates for each feature. Any such overlapping detections can be coalesced with standard methods for non-maximum suppression [?]. The center of each resulting rectangle constitutes an estimate for the associated feature’s position in the focal plane.

Convolutional neural networks also solve image recognition tasks through convolutions with selected kernels. In this case, the convolutions are integrated

into the network’s multi-layered, feed-forward architecture [?] and employ kernels that are designed and optimized during training. Constructing a CNN to perform general image classification requires massive computational resources [?]. Once constructed, however, a CNN can be retrained easily to recognize particular features of interest. Our application of CNNs for feature localization is based on TensorBox [?], an open-source package built on the GoogLeNet-OverFeat network [?], specifically on Inception v1 [?]. Tensorbox provides a convenient interface for training the input layers of Inception to recognize features of interest and the for training the output layers to associate these features with regression estimates for the locations and extents of detected features.

Both types of supervised machine-learning algorithms require sets of sample data for training and validation. Each training element consists of an image containing zero, one or more features together with a “ground truth” annotation for each feature in that image specifying the features’ locations and extents. Normally, these images are obtained experimentally and are annotated by hand. We instead train with synthetic holograms that are computed with the same light scattering theory [1] used to analyze experimental holograms. Using the physics of image formation for the ground truth for training eliminates the effort and errors inherent in empirical annotation.

4.3 Holographic Image Formation

Referring to Fig. 4.1, we model the holographic microscope’s illumination as a plane wave at frequency ω propagating down the \hat{z} axis (along $-\hat{z}$) and linearly

polarized along \hat{x} :

$$\mathbf{E}_0(\mathbf{r}, t) = u_0 e^{ikz} e^{i\omega t} \hat{x}, \quad (4.1)$$

where $k = n_m \omega / c$ is the wavenumber of the light in a medium of refractive index n_m . A particle at position \mathbf{r}_p scatters the incident wave, thereby creating the scattered field

$$\mathbf{E}_s(\mathbf{r}, t) = u_0 e^{ikz_p} \mathbf{f}_s(k[\mathbf{r} - \mathbf{r}_p]) e^{i\omega t}, \quad (4.2)$$

where $\mathbf{f}_s(k\mathbf{r})$ is the Lorenz-Mie scattering function [10, 11]. For the particular case of scattering by a sphere, $\mathbf{f}_s(k\mathbf{r})$ is parameterized by the sphere's radius a_p and refractive index n_p [10]. The field that reaches point \mathbf{r} in the focal plane ($z = 0$) is the superposition of these two contributions,

$$\mathbf{E}(\mathbf{r}, t) = \mathbf{E}_0(\mathbf{r}, t) + \mathbf{E}_s(\mathbf{r}, t). \quad (4.3)$$

The dimensionless intensity, $b(\mathbf{r}) \equiv u_0^{-2} |\mathbf{E}(\mathbf{r}, t)|^2$, is then given by

$$b(\mathbf{r}) = |\hat{x} + e^{ikz_p} \mathbf{f}_s(k[\mathbf{r} - \mathbf{r}_p])|^2. \quad (4.4)$$

In addition to a_p and n_p , this model for the image formation process depends on a small number of parameters that characterize the instrument. Our holographic microscope is powered by a 15 mW fiber-coupled diode laser (Coherent Cube) operating at a vacuum wavelength of $\lambda = 447$ nm. The combination of a half-wave plate and a polarizing beam splitter reduces the power incident on the sample to 3 mW and ensures that the light is linearly polarized along \hat{x} , as required by Eq. (4.4). A 100 \times oil-immersion objective lens (Nikon S-Plan

Apo, numerical aperture 1.3) and a matched 200 mm tube lens provide a total magnification of 135 nm/pixel on a standard video camera (NEC TI-324AII). The 640 pixel \times 480 pixel grid is digitized at 8 bits/pixel and recorded as uncompressed digital video at 29.97 frames/s with a commercial digital video recorder (Pioneer DVR-560H). The refractive index of the medium, n_m , is determined to within a part per ten thousand using an Abbe refractometer (Edmund Scientific).

Having determined the calibration constants, we treat the particle's position and properties as adjustable parameters and fit predictions of Eq. (4.4) to experimentally measured holograms. To do so, each video frame must first be corrected by subtracting off the camera's dark count [19], and then normalizing by the microscope's background intensity distribution [1]. Such fits typically yield a sphere's position with a precision of 1 nm in the plane and 3 nm axially [2, 7]. Characterization results are similarly precise, with the radius of a micrometer-diameter sphere typically being resolved to within 3 nm and the refractive index to within a part per thousand [4, 5].

This excellent performance requires starting estimates for the adjustable parameters that are good enough for the fitting algorithm to converge to a globally optimal solution. The fitter computes trial holograms according to Eq. (4.4), which is computationally expensive. It has to perform fewer of these computations when it is provided with better estimates for the starting parameters. Whereas heuristic localization algorithms meet this need, machine-learning algorithms are substantially faster and more robust, and can be comparably precise.

4.4 Applying Machine Learning to Holographic Particle Localization

We used Eq. (4.4) to generate training images of particles with radii ranging from $a_p = 0.25 \mu\text{m}$ to $5 \mu\text{m}$, refractive indexes from $n_p = 1.4$ to 2.5 , and axial positions from $z_p = 5 \mu\text{m}$ to $50 \mu\text{m}$. Each training hologram has parameters selected at random from this range and is centered at random within the field of view. Normalized experimental holograms have uncorrelated white noise that we model as additive Gaussian noise with a standard deviation of five percent.

Our cascade classifier was trained with 6000 synthetic images of colloidal spheres. These were combined with a complementary set of 4000 particle-free images recorded by the instrument itself. Each computed image is annotated with the coordinates of the corners defining that feature's region of interest. The region is centered on the feature's actual position and has an extent that encloses 10 interference fringes. The classifier was trained until its rate of false positive detections fell to 8×10^{-4} . This was achieved with a classifier that searches for features through five resolution stages, with each stage being comprised of a distinct set of five wavelets. This geometry and the choice of weak classifiers was arrived at by the training algorithm's optimizer.

The convolutional neural network was trained with 3000 synthetic holographic images; another 600 were used for validation. These images also were annotated with feature positions and extents drawn from the ground truth for the image-formation process. CNN training converged after 50 000 cycles of training and validation.

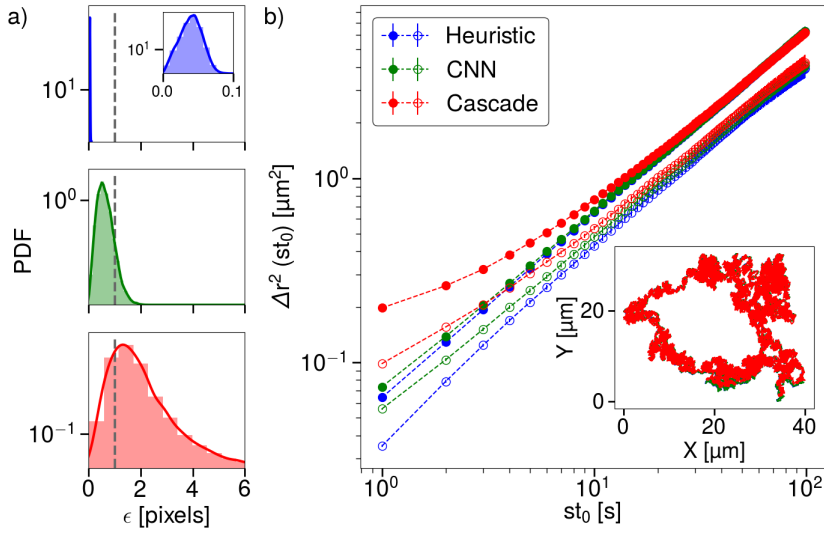


Fig. 4.2: Each localization technique provided estimates for the trajectory of a simulated brownian particle. (a) Probability distribution functions for the localization error achieved by (top) heuristic algorithm, (middle) convolutional neural network, and (bottom) cascade classifier. Inset shows expanded view of the sub-pixel resolution. Vertical dashed line indicates single-pixel precision. (b) Mean-square displacement computed from trajectories obtained with the three detection algorithms. Short-time asymptotes yield dynamical estimates for the localization error. Open circles represent experimental data, as explained in Sec. 4.4.4.

4.4.1 Precision and Accuracy

We assess the detectors' localization precision by comparing detection results with known input parameters. A typical example for a particular choice of particle properties is shown in Fig. 4.2. The three probability distributions in Fig. 4.2(a) present the root-mean-square localization error obtained by each of the algorithms when tracking particles with $a_p = 1.0 \mu\text{m}$ and $n_p = 1.5$. We generate data for these plots by simulating the diffusion of such a particle through water at

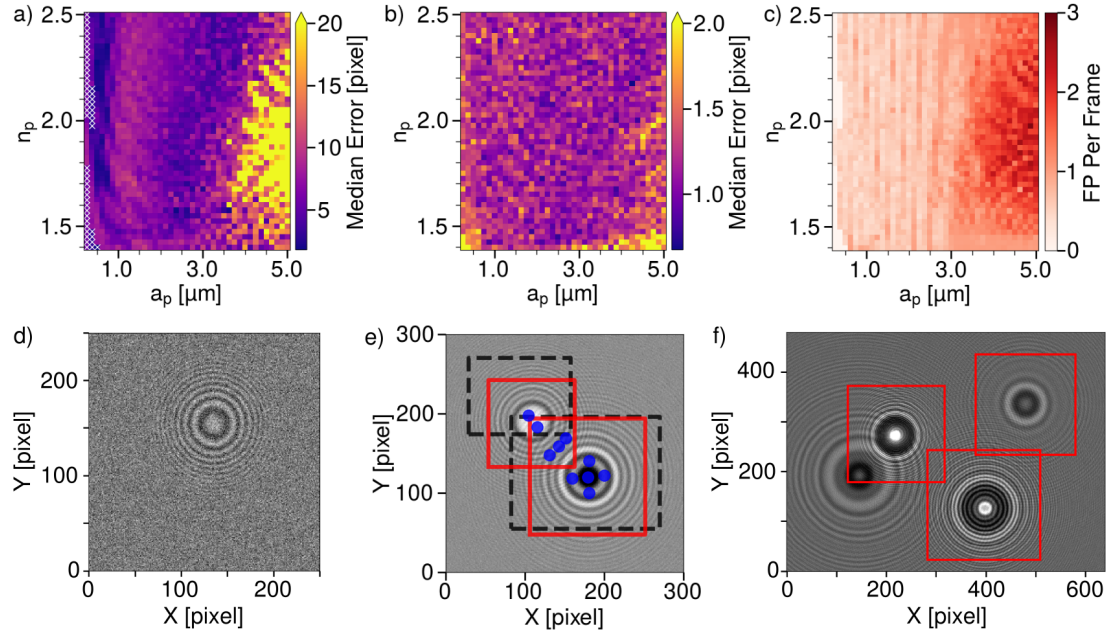


Fig. 4.3: Localization errors as a function of particle radius and refractive index at a height of $z_p = 13.5 \mu\text{m}$ above the focal plane. (a) Cascade classifier. (b) Convolutional neural network. (c) Rate of false positive detections for the cascade classifier. (d) Hologram of a 500 nm-diameter silica sphere that was overlooked by the cascade classifier. This particle was localized to within one pixel by the CNN. (e) Hologram of a 2.4 μm -diameter polystyrene sphere (upper left) interfering with the hologram of a 4.0 μm -diameter TPM sphere located 15 μm above it. Blue dots show feature locations proposed by the heuristic algorithm; Red boxes enclose features detected by the CNN; Dashed black boxes are proposed by the cascade classifier. (f) Hologram of four particles overlaid with regions of interest identified by the CNN. One occluded feature was overlooked by the CNN.

a temperature of 20 °C starting from the center of the field of view at $z_p = 13.5 \mu\text{m}$ and proceeding for 3000 steps at 33 ms per step.

The heuristic algorithm consistently yields sub-pixel precision with a median error of 0.04 pixels. The convolutional neural network also yields sub-pixel precision with a median localization error of 0.61 pixels. The cascade classifier performs less well, with a median localization error of 1.81 pixels and a substantial probability for errors extending to several pixels. For applications such as Lorenz-Mie microscopy that require input estimates with sub-pixel precision, the cascade classifier’s localization precision may not be sufficient.

The inset of Fig. 4.2(b) shows the trajectory reconstructed by each of the algorithms. The measured trajectory’s mean-squared displacement (MSD) provides an estimate for the particle’s diffusion coefficient. All three methods yield results that are consistent with the particle’s true diffusivity, $D = 0.482 \mu\text{m}^2/\text{s}$, which suggests that their localization errors are normally distributed. Extrapolating the MSD to zero lag time provides an estimate for the localization error [?, 26]. In all three cases, the extrapolated measurement error is consistent with the median values from Fig. 4.2(a).

Applying the same techniques across the entire range of particle sizes and refractive indexes yields results for the median localization error summarized in Fig. 4.3(a) and 4.3(b). Results from the cascade classifier in Fig. 4.3(a) range from single-pixel precision under most conditions to more than 20 pixels for the largest spheres we considered. These errors are dominated by the cascade classifier’s tendency to displace location estimates toward the center of the field of view when presented with features that extend outside the observation window. This

problem is more pronounced for the larger holographic features created by larger scatterers. Smaller particles create holograms with low signal-to-noise ratio that can be overlooked by the cascade classifier, leading to false negative detections. Such conditions are indicated by white crosses in Fig. 4.3(a). A typical example of such a challenging hologram is shown in Fig. 4.3(d).

The results plotted in Fig. 4.3(b) show that the CNN yields much smaller localization errors than the cascade classifier. The CNN achieves sub-pixel resolution over the entire range of parameters, although localization precision is worse for weak scatterers and large spheres. Unlike the cascade classifier, it returned no false negative results, and even achieved single-pixel precision for the low-contrast hologram in Fig. 4.3(d).

Both the cascade classifier and the CNN return a small rate of false positive detections. Figure 4.3(c) reports the false-positive rate for the cascade classifier, which ranges from 10^{-1} frame $^{-1}$ for holograms of particles with $a_p < 3 \mu\text{m}$ to 3 frame $^{-1}$ for holograms of larger spheres. In all cases, these false positive detections come in addition to the correct particle detection, and result from the classifier's failure to correctly coalesce multiple detections of the same particle. Such false positive detections contribute to the very large localization error for large spheres in Fig. 4.3(a). The CNN performs substantially better, with fewer than one false positive per thousand frames.

4.4.2 Multiple Particles

The results presented so far apply to holograms of single particles. In practice, it is not unusual for multiple particles to enter the microscope's field of view

simultaneously. Their scattering patterns interfere to create intensity variations that can confuse heuristic detection algorithms. Depending on the particles' proximity and alignment, their holograms can merge into irregular patterns whose analysis requires more specialized techniques [?, 17]. The hologram in Fig. 4.3(e) illustrates the effect of more modest overlap. It captures a 2.4 μm -diameter polystyrene sphere 17 μm above the focal plane whose hologram is partially occluded by that of a 4.0 μm -diameter TPM sphere situated 15 μm above and 15 μm off to the side. Discrete points overlaid on this image show the positions that the heuristic algorithm identified as centers of candidate features. Of the 10 proposed features, 8 are false positive detections and one is poorly localized.

Both machine-learning algorithms perform better than the heuristic algorithm for this image. The cascade classifier correctly detects both particles, as indicated by dashed rectangles in Fig. 4.3(d). The estimated locations, however, are displaced significantly from the features' true centers, presumably because of interference between the two scattering patterns. The CNN not only detects and localizes both particles correctly, but also provides useful estimates for the extent of the scattering patterns, as denoted by the solid (red) squares overlaid on Fig. 4.3(d).

More substantial overlap can confound the CNN, leading to false-negative detections. Figure 4.3(f) shows a hologram with overlapping features due to four spheres located in four different planes over a 50 μm axial range. The CNN correctly detects and localizes three particles, and provides reasonable estimates for their features' extents. The fourth feature, which is larger and has lower contrast, is omitted. Such false negatives become more common as the number and extent of

features in a hologram increases. Standard bright-field imaging would miss even more of these particles because the axial range over which they are distributed greatly exceeds a conventional microscope’s depth of focus.

These results illustrate that machine-learning algorithms can be more reliable than heuristic algorithms for detecting and localizing features in non-ideal holograms. For applications such as monitoring colloidal concentrations, this benefit alone might recommend machine-learning algorithms over other approaches. The principal benefit of machine-learning algorithms, however, is their ability to detect features rapidly, even on low-power computational platforms.

4.4.3 Computation Speed

Table 4.1 presents timing data for holographic feature detection on a 1 Gflops desktop workstation outfitted with an nVidia GTX 680 GPU. This system can detect a single feature in just under 700 ms using the heuristic algorithm described in Sec. 4.2.1. Of this, 150 ms is required for the orientation alignment

Table 4.1: Analysis times in ms/frame for the heuristic algorithm, the convolutional neural network (CNN) implemented on CPU and GPU, and the cascade classifier implemented on a workstation and on a Raspberry Pi 3 single-board computer.

	Mean [ms]	Median [ms]	Std. [ms]	Min [ms]	Max [ms]
Heuristic (CPU)	695	700	11	670	1000
CNN (CPU)	278	278	2.8	271	315
CNN (GPU)	52	52	4.8	50	70
Cascade (CPU)	17	17	1.0	15	81
Cascade (RPi)	173	171	12	159	275

transform and half a second is required to analyze the transformed image and then to detect and localize its peaks. This bottleneck can be reduced to 50 ms by specifying the anticipated width, height and separation of the transformed peaks. In this case, the present implementation’s processing speed is consistent with previous reports [?, 1, 7] when account is taken of image size and processor speed. No single set of such parameters, however, successfully detects features over the entire range of parameters considered in Fig. 4.3. The slow operation reported in Table 4.1 therefore represents the cost of generality.

The CNN routinely outperforms the heuristic algorithm by a factor of 2.5 on the same hardware over the entire range of parameters. Transferring the CNN calculation to the GPU increases this advantage to a factor of 11. Most remarkably, the cascade classifier is 40 times faster than the reference heuristic algorithms, even without GPU acceleration, processing features fast enough to keep up with the 33 ms frame rate of a standard video camera.

The cascade classifier is so computationally efficient that it can be deployed usefully on a lightweight embedded computer. We demonstrated this by analyzing holograms on a Raspberry Pi 3 single-board computer. Even though the lightweight computer runs the cascade classifier 10 times slower than the workstation, it is still 4 times faster than the heuristic algorithms on the workstation. Reducing the resolution by half, improves the Raspberry Pi’s detection time to 40 ms per image which corresponds to 25 frames/s.

4.4.4 Experimental Demonstrations

Real-time detection of holographic features has applications beyond holographic particle characterization. The implementations presented here are suitable for targeting optical traps in holographic trapping systems [27]. We have demonstrated this by integrating machine-learning particle detection into an automated trapping system that projects optical traps onto the particles' positions to acquire them for subsequent processing. Pioneering implementations of automated trapping [?] rely on conventional imaging and so require target particles to lie near the microscope's focal plane. Holographic targeting works over a much larger axial range. Both the CNN and the cascade classifier locate particles in the plane

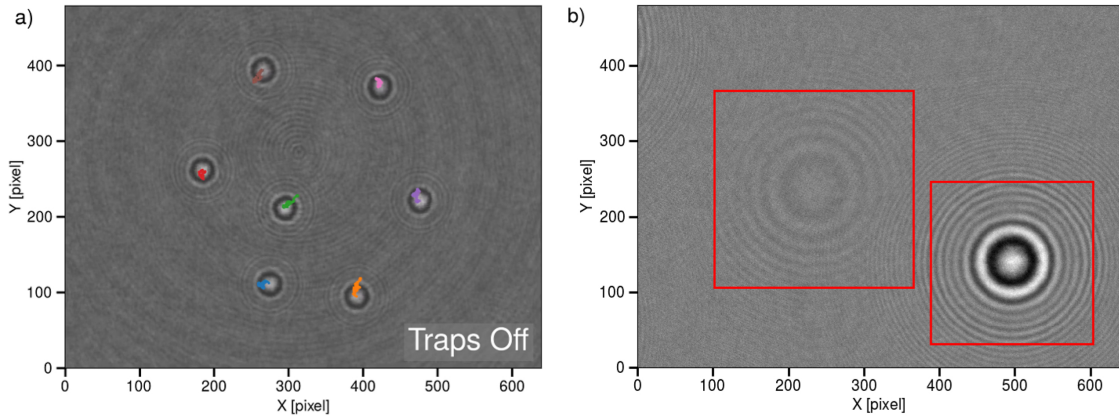


Fig. 4.4: (a) Cascade classifier tracking 2 μm -diameter colloidal spheres diffusing through water in a holographic optical trapping system. Each trace shows 5 seconds of the associated particle's motion. The associated video (Visualization 1) shows the tracking data being used to alternately trap and release the particles. (b) CNN detection of holographic features. The high-contrast feature is created by a 1.5 μm diameter silica sphere. The low-contrast feature represents a coliform bacterium in the dispersion.

with sufficient precision to ensure reliable trapping. The axial coordinate required for three-dimensional targeting can be extracted from holographic features using previously reported techniques [16]. Because of its speed, the cascade classifier is particularly useful for targeting fast-moving particles. Figure 4.4(a) shows the cascade classifier tracking colloidal particles in real time as they diffuse in a holographic trapping system. The instrument uses this tracking information to trap the detected particles, as shown in the associated video (Visualization 1).

Figure 4.4(b) shows typical results obtained with the CNN analyzing experimental data. The image is a normalized hologram of a $1.5\text{ }\mu\text{m}$ -diameter silica sphere dispersed in water flowing down a $100\text{ }\mu\text{m}$ -deep microfluidic channel. The second holographic feature in this image is due to a coliform bacterium in the sample [?]. The CNN detects and correctly localizes both features despite their substantial difference in contrast.

We can estimate the feature-detection algorithms' precision for particle localization by tracking diffusing particles [26]. The open circles in Fig. 4.2(b) show results obtained with heuristic and machine-learning algorithms for the mean-square displacement of a single colloidal polystyrene sphere (Duke Scientific, catalog no. 4016A, nominal diameter $1.587 \pm 0.018\text{ }\mu\text{m}$) diffusing through water at room temperature. Because polystyrene is 5 % more dense than water, the particle sediments $11\text{ }\mu\text{m}$ over the course of this 3 min measurement. In all three cases, the in-plane localization error obtained by extrapolating these results is consistent with that reported for synthetic data.

4.5 Discussion

The use of machine-learning algorithms for detecting and localizing holographic features enable and enhance a host of applications for holographic video microscopy. CNNs detect and localize colloidal particles faster than conventional image-analysis techniques and localize particles well enough for subsequent processing. Our implementation also estimates the extent of each holographic feature thereby bypassing the standard next step in Lorenz-Mie microscopy [7] and saving additional time. These substantial speed enhancements make it possible to perform holographic particle characterization measurements in real time rather than requiring off-line processing. CNNs also are more successful at interpreting overlapping features in multi-particle holograms and thus can be used to analyze more concentrated suspensions.

The Haar-based cascade classifier also outstrips the heuristic algorithms' ability to detect colloidal particles, particularly in heterogeneous samples and crowded fields of view. Although it cannot match the localization precision of CNNs, its speed and modest computational requirements create new opportunities. We have deployed our cascade classifier on a light-weight single-board computer and have demonstrated its utility for counting particles and thus for measuring colloidal concentrations. Such a low-cost instrument should be useful for routine monitoring of industrial processes and products and for environmental monitoring. We also have demonstrated the cascade classifier's utility for high-speed targeting in holographic trapping. In this case, speed is more important than localization precision for interacting with processes as they unfold.

While the present study focuses on detecting and localizing holographic

features with radial symmetry, the machine-learning framework can be applied equally well to asymmetric holograms produced by rods, clusters or biological samples. By reducing the computational burden of analyzing holograms, machine-learning algorithms extend the reach of holographic tracking and holographic characterization. More generally, machine-learning algorithms are well-suited to bootstrapping the more detailed analysis involved in holographic particle characterization. We anticipate that more of these physics-based processing steps will be taken over by machine-learning algorithms as that technology advances.

Open-source software for holographic particle tracking and characterization is available online at <https://github.com/davidgrier/>.

Chapter 5

Optimizing the synthesis of monodisperse colloidal spheres

Since the introduction of emulsion polymerization in XXX [XXX citation], synthesis of colloidal spheres has progressed through intuitive leaps guided by fundamental principles of chemistry and physics. Quite often, the importance of particular chemical or physical conditions to the outcome can only be gauged once synthesis is complete, and requires multiple orthogonal measurement techniques. Examples include measurements of the size distribution of their particles, their surface texture, and their porosity. Here, we explore the role of stoichiometry, initiator choice and agitation conditions on the synthesis of monodisperse spheres of 3-methacryloxypropyltrimethoxysilane (TPM), a model system with increasingly widespread applications in soft-matter research [XXX anything else?]. We employ holographic particle characterization in tandem with conventional particle characterization techniques to identify factors that influence size selection, polydispersity

and surface texture.

Spheres made from 3-methacryloxypropyltrimethoxysilane (TPM) are a particularly useful system for colloidal studies. Their synthesis readily produces monodisperse spheres in a wide range of sizes through a process that is simpler than that for other common colloidal particles, such as polystyrene and silica. There is no specialized equipment or inert environment necessary. The particles can be made in a single step through an order of magnitude of sizes, from a few hundred nanometers to a few micrometers. However, there are many parameters in the synthesis that can affect the final particle that is produced. In this study we vary a selection of these conditions and use holographic video microscopy to observe how they affect the final product of the synthesis.

5.1 Experimental Section

5.1.1 Materials.

TPM OIL (what and purchased from where). Ammonia. Initiators. Stir bars. Vials (microcentrifuge). Heat/shaker. tubes. xCells xSight.

5.1.2 Emulsification Polymerization.

All of the spheres in this study were made through an emulsion polymerization process. Monomeric TPM, which is insoluble in water, is added to a basic environment ($\text{pH} > 9$) of ammonia in water. The monomers undergo hydrolysis in the water and become water soluble. In a basic environment, these hydrolyzed

monomers form insoluble oligomers. As the suspension is stirred, the oligomers condense homogeneously into monodisperse droplets that grow as more oligomers form. After 2 hours, this process is completed and the droplets have reached their final size. Once the droplets are formed, a free radical initiator is used to polymerize the droplets and form solid spheres.

The droplet formation is done in a closed vial to prevent the evaporation of the ammonia and maintain the pH throughout the droplet formation process. This suggests that the particular container used for the synthesis may affect the final product, as the amount of air above the suspension will affect how much ammonia is left in the water and therefore the pH of the environment. To control this, we used identical 12 mL vials to make 5 mL of colloidal suspension in each synthesis.

First, we investigate the effect of varying the stir speed of the suspensions during droplet formation. In four identical vials with identical stir bars, we 15 mL of 29 % ammonia followed by 200 μ L of TPM monomer to 5 mL of DI water. The four samples are then stirred using magnetic stir plates set at 500, 700, 900, and 1100 min^{-1} for 2 h. At this point the droplets have stopped growing and they are polymerized by adding 2,2'-azobis(2-methylpropionitrile) (AIBN) and heating to 80 °C for 2 h.

The polymerization of the TPM droplets can be tracked by observing the refractive index of the particles over time. As the droplets polymerize, their refractive index increases until they are fully polymerized. To track this, we sampled the suspension above that was stirred at 1100 min^{-1} after 5, 10, 15, 20, 40, and 60 min of heating and measured the particles' refractive index.

Next, we observe the effect of using different free radical initiators to polymerize the particles. Two water-insoluble initiators, AIBN and 1,1'-azobis(cyclohexanecarbonitrile) (ACHN), and two water-soluble initiators, potassium persulfate (KPS) and ammonium persulfate APS), were used. To do this, one suspension of emulsion droplets is made and then divided into four vials. Each vial was then polymerized at 80 °C for 12 h on a shaker at 750 min⁻¹ to prevent sedimentation. We repeated this process with four different emulsions for a total of 16 measurements to ensure that any observations were the result of the initiator and not of the particular protocol used to make the emulsion.

To make the four batches of droplets, we hold the volume of water constant and vary the amounts of TPM and ammonia. Batches A and B each had 100 µL of TPM with 10 and 20 µL of ammonia added, respectively. Batches C and D had 150 µL, again with 10 and 20 µL of ammonia, respectively. The polymerization for all of the particles was done in 0.1 % SDS to avoid aggregation.

In making the 16 sets of particles to look at the effect of initiator on the particles, we can also make observations about the effects of varying the amount of TPM and the pH on the size of the resulting droplets. To hold the pH constant, we can compare sample A to C and sample B to D. This gives the fairly intuitive result that increasing the amount of TPM increases the size of the final droplet. Holding the amount of TPM constant and varying the pH, which means comparing A to B and C to D, shows that increasing the pH of the environment during droplet formation decreases the size of the final droplet. This is less intuitive but perhaps not surprising, as the pH affects the rate at which oligomers form and therefore the rate of droplet formation. This leads to more nucleation sites and therefore

smaller droplets for the same volume of material.

5.1.3 Characterization

5.2 Results and discussion

5.2.1 Role of Initiator.

5.2.2 Role of Heat Bath.

5.2.3 Role of Stir rate.

5.3 Conclusion

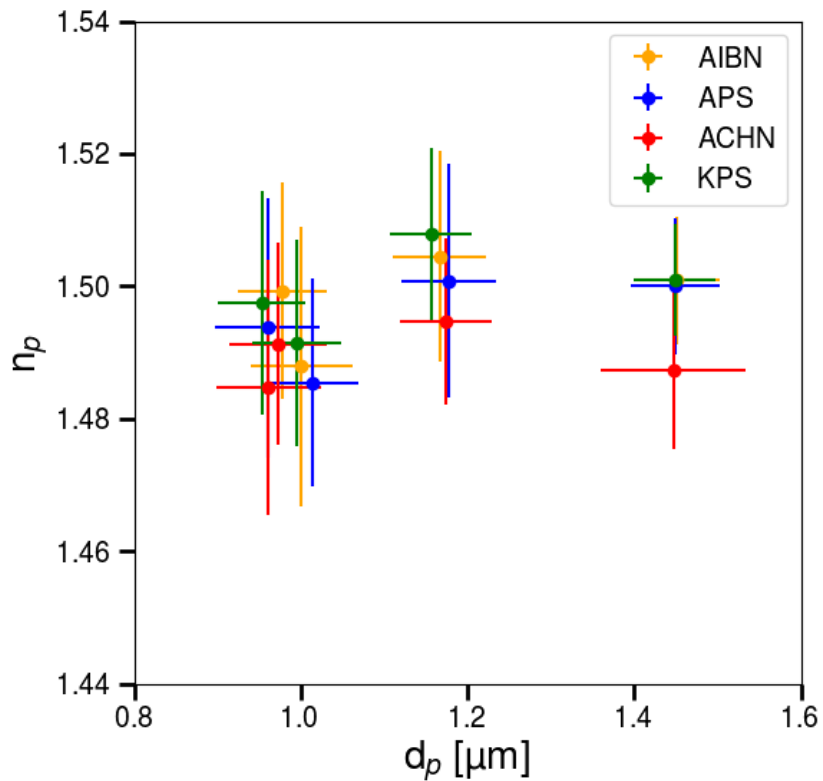


Fig. 5.1: The refractive index and diameter of 16 samples of polymerized TPM.

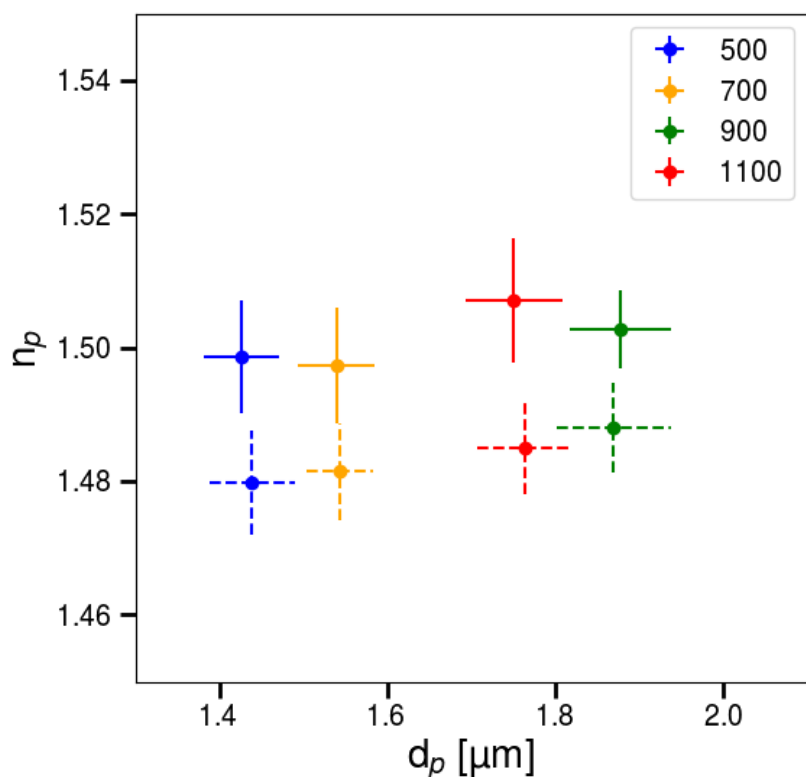


Fig. 5.2: Caption

Chapter 6

Conclusions

Bibliography

- [1] Sang-Hyuk Lee, Yohai Roichman, Gi-Ra Yi, Shin-Hyun Kim, Seung-Man Yang, Alfons van Blaaderen, Peter van Oostrum, and David G. Grier. Characterizing and tracking single colloidal particles with video holographic microscopy. *Opt. Express*, 15:18275–18282, 2007.
- [2] Fook Chiong Cheong, Bhaskar Jyoti Krishnatreya, and David G. Grier. Strategies for three-dimensional particle tracking with holographic video microscopy. *Opt. Express*, 18:13563–13573, 2010.
- [3] Henrique Moyses, Bhaskar Jyoti Krishnatreya, and David G. Grier. Robustness of holographic video microscopy against defects in illumination. *Opt. Express*, 21:5968–5973, 2013.
- [4] Bhaskar Jyoti Krishnatreya, Arielle Colen-Landy, Paige Hasebe, Breanna A. Bell, Jasmine R. Jones, Anderson Sunda-Meya, and David G. Grier. Measuring boltzmann’s constant through holographic video microscopy of a single sphere. *Am. J. Phys.*, 82:23–31, 2014.
- [5] Hagay Shpaisman, Bhaskar Jyoti Krishnatreya, and David G. Grier. Holographic microrefractometer. *Appl. Phys. Lett.*, 101:091102, 2012.

- [6] Sang-Hyuk Lee and David G Grier. Holographic microscopy of holographically trapped three-dimensional structures. *Opt. Express*, 15:1505–1512, 2007.
- [7] Fook Chiong Cheong, Bo Sun, Rémi Dreyfus, Jesse Amato-Grill, Ke Xiao, Lisa Dixon, and David G. Grier. Flow visualization and flow cytometry with holographic video microscopy. *Opt. Express*, 17:13071–13079, 2009.
- [8] Lisa Dixon, Fook Chiong Cheong, and David G. Grier. Holographic particle-streak velocimetry. *Opt. Express*, 19:4393–4398, 2011.
- [9] Bhaskar Jyoti Krishnatreya and David G. Grier. Fast feature identification for holographic tracking: The orientation alignment transform. *Opt. Express*, 22:12773–12778, 2014.
- [10] Craig F. Bohren and Donald R. Huffman. *Absorption and Scattering of Light by Small Particles*. Wiley Interscience, New York, 1983.
- [11] M. I. Mishchenko, L. D. Travis, and A. A. Lacis. *Scattering, Absorption and Emission of Light by Small Particles*. Cambridge University Press, Cambridge, 2001.
- [12] Eric R. Dufresne and David G. Grier. Optical tweezer arrays and optical substrates created with diffractive optical elements. *Rev. Sci. Instrum.*, 69(5):1974–1977, 1998.
- [13] Bruce T. Draine and Piotr J. Flatau. Discrete-dipole approximation for scattering calculations. *Journal of the Optical Society of America A*, 11(4):1491–1499, 1994.
- [14] J. Fung, R. W. Perry, T. G. Dimiduk, and V. N. Manoharan. Imaging multiple colloidal particles by fitting electromagnetic scattering solutions to digital

- holograms. *J. Quant. Spectr. Rad. Trans.*, 113:2482–2489, 2012.
- [15] Jian Sheng, Edwin Malkiel, and Joseph Katz. Digital holographic microscope for measuring three-dimensional particle distributions and motions. *Appl. Opt.*, 45(16):3893–3901, 2006.
- [16] Aaron Yevick, Mark Hannel, and David G. Grier. Machine-learning approach to holographic particle characterization. *Opt. Express*, 22:26884–26890, 2014.
- [17] R. W. Perry, G. N. Meng, T. G. Dimiduk, J. Fung, and V. N. Manoharan. Real-space studies of the structure and dynamics of self-assembled colloidal clusters. *Faraday Discuss.*, 159:211–234, 2012.
- [18] Chen Wang, Xiao Zhong, David B. Ruffner, Alexandra Stutt, Laura A. Philips, Michael D. Ward, and David G. Grier. Holographic characterization of protein aggregates. *J. Pharm. Sci.*, 105:1074–1085, 2016.
- [19] Chen Wang, Fook Chiong Cheong, David B Ruffner, Xiao Zhong, Michael D Ward, and David G Grier. Holographic characterization of colloidal fractal aggregates. *Soft Matter*, 12(42):8774–8780, 2016.
- [20] Fook Chiong Cheong and David G Grier. Rotational and translational diffusion of copper oxide nanorods measured with holographic video microscopy. *Optics Express*, 18(7):6555–6562, 2010.
- [21] Mark Hannel, Christine Middleton, and David G. Grier. Holographic characterization of imperfect colloidal spheres. *Appl. Phys. Lett.*, 107:141905, 2015.
- [22] Chen Wang, Hagay Shpaisman, Andrew D. Hollingsworth, and David G. Grier. Monitoring colloidal growth with holographic microscopy. *Soft Matter*, 11:1062–1066, 2015.

- [23] Chen Wang, Henrique W. Moyses, and David G. Grier. Stimulus-responsive colloidal sensors with fast holographic readout. *Appl. Phys. Lett.*, 107:051903, 2015.
- [24] Fook Chiong Cheong, Ke Xiao, David J. Pine, and David G. Grier. Holographic characterization of individual colloidal spheres' porosities. *Soft Matter*, 7:6816–6819, 2011.
- [25] Fook Chiong Cheong, Simone Duarte, Sang-Hyuk Lee, and David G. Grier. Holographic microrheology of polysaccharides from streptococcus mutans biofilms. *Rheologica Acta*, 48(1):109–115, 2009.
- [26] John C. Crocker and David G. Grier. Methods of digital video microscopy for colloidal studies. *J. Colloid Interface Sci.*, 179:298–310, 1996.
- [27] David G. Grier. A revolution in optical manipulation. *Nature*, 424(6950):810–816, 2003.